Arabian Journal for Science and Engineering (2022) 47:4059–4077
https://doi.org/10.1007/s13369-021-05853-8

RESEARCH ARTICLE-CIVIL ENGINEERING

Investigation of Surface Settlement and Wall Deflection Caused by Braced Excavation in Spatially Variable Clays Based on Anisotropic Random Fields

Shun Yi[1,2,3,4] · Jian Chen[1,2,3,4,5,6] · Juehao Huang[1,2,3,4] · Jianbin Li[7] · Yuefeng Qiu[1,2] · Weijun You[8]

Received: 4 February 2021 / Accepted: 9 June 2021 / Published online: 24 June 2021

Abstract

This research aims to assess the influences of the spatial variability of soil parameters on the ground surface and retaining wall deformation induced by braced excavation. A series of anisotropic random fields are generated and used for the finite difference analysis in this paper. A procedure for automating the Monte Carlo simulation is employed to ascertain the influences of coefficient of variation and scale of fluctuation (*SOF*) of soil stiffness parameters on the excavation-induced responses. In addition, the effects of horizontal *SOF* and vertical *SOF* are distinguished in the anisotropic framework. The stochastic results indicate that the presented computational framework is effective in the investigation of excavation-induced deformations. Further probabilistic analyses are performed to evaluate the failure probabilities of surface settlement (SS) and retaining wall deflection (RWD). This study shows the importance of addressing the spatial variability of stiffness parameters for soil and structure problems. A series of modes for SS and RWD are presented with consideration of the effects of weak stiffness regions. The effects of vertical *SOF* on excavation-induced deformations are larger than those of horizontal *SOF*. The concept of vertical *SOF* correlation is proposed to explain that the most scattered result occurs when the vertical *SOF* is close to the size of the excavation. The research can provide a beneficial reference for advance warning of failure or hazard when performing probabilistic assessment of excavation-induced deformations.

Keywords Spatial variability · Anisotropic random field · Surface settlement · Retaining wall deflection · Probabilistic analyses

List of Symbols

SS	Surface settlement
RWD	Retaining wall deflection
SLS	Serviceability limit state
SOF, SOFs	Scale of fluctuation
COV, COVs	Coefficients of variability
PH-SS model	The plastic hardening-small-strain model
CMDM	The covariance matrix decomposition method
ACF	Auto-correlation function

✉ Jian Chen
chenjian@whrsm.ac.cn

Shun Yi
sunyee_123@163.com

[1] State Key Laboratory of Geomechanics and Geotechnical Engineering, Institute of Rock and Soil Mechanics, Chinese Academy of Sciences, Wuhan 430071, People's Republic of China

[2] School of Engineering Science, University of Chinese Academy of Sciences, Beijing 100049, People's Republic of China

[3] Hubei Key Laboratory of Geo-Environmental Engineering, Institute of Rock and Soil Mechanics, Chinese Academy of Sciences, Wuhan 430071, People's Republic of China

[4] State Key Laboratory of Geomechanics and Geotechnical Engineering, Soft Soil Research Center, Ningbo University of Technology, Ningbo 315211, People's Republic of China

[5] China-Pakistan Joint Research Center on Earth Sciences, Islamabad, Pakistan

[6] National-Local Joint Engineering Research Center of Underwater Tunnelling Technology, Wuhan 430063, People's Republic of China

[7] School of Civil Engineering, Guangzhou University, Guangzhou 510006, People's Republic of China

[8] China Construction Third Bureau First Engineering Co., LTD, Wuhan 430000, People's Republic of China

MCS	Monte Carlo simulation
LSF	The limit state function
RFDM	Random finite difference method
F_s	The factor of safety against basal heave
q_a	The asymptotic value of the deviatoric stress
q	The deviatoric stress
E_i	The initial soil Young's modulus at a very low-strain ($<10^{-6}$)
G_0	The initial or very small-strain shear modulus
G	The shear modulus
$\gamma_{0.7}$	The shear strain at which $G=0.7G_0$
γ	The shear strain
ε_1	The axial (vertical compressional) strain
$E_{\mathrm{oed}}^{\mathrm{ref}}$	Tangent stiffness for primary oedometer loading (kN/m^2)
E_{50}^{ref}	Secant stiffness in standard drained triaxial test (kN/m^2)
$E_{\mathrm{ur}}^{\mathrm{ref}}$	Unloading/reloading stiffness at engineering strains (kN/m^2)
G_0^{ref}	Reference shear modulus at very small strains ($<10^{-6}$) (kN/m^2)
φ'	Effective angle of internal friction (°)
c'	Effective cohesion (kN/m^2)
υ	Poisson's ratio
m	Exponent of the stress-dependency of stiffness
p^{ref}	Reference stress for stiffnesses (kN/m^2)
τ_x	The absolute distance between any two spatial points in the horizontal direction (m)
τ_z	The absolute distance between any two spatial points in the vertical direction (m)
θ_x	The horizontal SOFs (m)
θ_z	The vertical SOFs (m)
$\rho(\tau_x, \tau_z)$	The auto-correlation coefficient between any two spatial points
$C_{n\times n}$	The auto-correlation matrix
L	A lower triangular matrix
L^T	The transpose of the matrix L
Y	A randomly generated vector
P_{f}	The probability of failure
Z	The limit state function (LSF)
S_{sto}	The response of stochastic calculation
S_{lim}	The limiting value of the corresponding response
N	The number of MCSs
$I[-]$	The indicator function. When $Z<0$, $I[-]$ is 1, otherwise zero
K_{n}	The normal stiffness (kN/m^2)
K_{s}	The shear stiffness (kN/m^2)
K	The average value of the soil bulk stiffness (kN/m^2)
G	The average value of the soil shear stiffness (kN/m^2)
Δz	The element size on the low-stiffness side in the adjacent soil element
H	The final depth of excavation (m)
B	The half-width of excavation (m)
$\mu_{\ln}$	Mean of the lognormal distribution
$\sigma_{\ln}$	Standard deviation of the lognormal distribution
μ	Mean of the normal distribution
σ	Standard deviation of the normal distribution
δ_{vm}/H	The dimensionless parameter for maximum SS
δ_{hm}/H	The dimensionless parameter for maximum RWD

1 Introduction

With the population of major cities increasing, more underground engineering works are under construction or will be constructed in the near future. Braced excavation has been used widely. During the advance of an excavation, the retaining wall deflection (RWD) and surface settlement (SS) are the key reference to evaluate the safety conditions of underground engineering works and prevent the excavation from failure. In general, the maximum RWD and maximum SS caused by excavation are determined using serviceability limit state (SLS) design [1] and need to satisfy the limiting values specified by the local regulatory agency. Table 1demonstrates an example of criteria for excavation-induced responses in Shanghai, China, according to the 'Specification for excavation in Shanghai metro construction' [2]. Thus, it is necessary to predict the maximum RWD and SS during the design of a braced excavation.

It is acknowledged that the values of soil parameters exert a significant influence on the soil/wall deformation caused

Table 1 Criteria for the limiting values of excavation-induced responses in Shanghai, China [2]

Excavation protection level	Limiting values of excavation-induced responses		
	Maximum retaining wall deflection	Maximum surface settlement	F_S (basal stability)
I	$\leq 0.14\%\ H$	$\leq 0.1\%\ H$	≥ 2.2
II	$\leq 0.3\%\ H$	$\leq 0.2\%\ H$	≥ 2.0
III	$\leq 0.7\%\ H$	$\leq 0.5\%\ H$	≥ 1.5

H represents the excavation depth; F_s is the factor of safety against basal heave by excavations. Thus, it is important to describe the soil parameters accurately. Numerous attempts [3–5] have been made to investigate the responses induced by excavations, but limitations exist in these methods in that soils are usually considered as isotropic and homogeneous materials. In reality, uncertainty prevails in geotechnical engineering. Morgenstern [6] divided this uncertainty into three categories: parameter uncertainty, model uncertainty, and human factor uncertainty. Among them, research into geotechnical parameters shows that the parameter uncertainty mainly results from the spatial variability. In this regard, Lumb [7] proposed the concept of 'spatial variability' of soil parameters and demonstrated that the spatial variability is attributed to the difference in material composition during the sedimentation process and the effects of various uncertain external forces later in the period. Vanmarcke [8] treated soil parameters as a random field and established a random field model encompassing spatial variability. Using the random field model, many studies have been conducted and reported foci include, e.g., foundation settlement [9], ground movements caused by tunneling [10], and slope stability [11, 12]. Recently, the random field model is also employed in the field of braced excavations. Luo et al. [13] assessed the influences of soil spatial variability on excavation-induced responses and identified the possibility of geotechnical and structural failure in engineering design. Ching et al. [14] explored the phenomenon of a worst-case scale of fluctuation (*SOF*) in basal heave analysis for excavation in spatially variable clays. Gholampour and Johari [15] developed a beneficial method for reliability-based analysis of braced excavation considering the uncertainties involved in the soil–structure interaction. Sert et al. [16] implemented random finite element modeling (RFEM) to estimate the wall deflection and bending moment of the retaining wall with consideration of the spatial variations of the effective friction angle φ'. Lo and Leung [17] proposed an approach to obtain improved predictions for a braced excavation on the basis of the Bayesian updating of subsurface spatial variability. According to the aforementioned studies on soil parameters spatial variability, some beneficial works have been conducted in relation to excavations: However, it is noteworthy that most existing studies considering soil parameter spatial variability focus on the isotropic spatial variability, which is inconsistent with site conditions. In reality, anisotropic spatial variability prevails in site. In the framework of anisotropy random fields, the horizontal *SOF* of soil parameter variability is different from their vertical *SOF* [18–20]. It is necessary to assess the influences of anisotropic spatial variability on the excavation-induced deformation responses.

In reality, the anisotropy of soft clay has been considered in geotechnical engineering [21–26]. Many attempts have been also made for excavation analyses considering the clay anisotropy: n, ground settlement [27], wall deflection [28], earth pressure [29], and basal heave stability [30–32]. It is noted that most of these literature adopted the NGI-ADP model [25], which is an anisotropy shear strength for clay using nonlinear stress path-dependent hardening relationship. In this regard, the random field in the framework of anisotropy structure is rarely reported in the investigations of excavation-induced responses. In addition, with respect to different mechanisms of RWD and SS caused by braced excavation, it remains to be described and explained. Meanwhile, the effects of the anisotropy soil on the probability of failure for RWD and SS should also be investigated in the study of braced excavation-induced responses.

In this paper, the effects of soil parameter spatial variability on the deformation assessments of braced excavation are ascertained, with consideration of anisotropic correlation structures. In the framework of Monte Carlo simulation (MCS), the study establishes anisotropy random field models to evaluate the influences of coefficients of variability (*COVs*) and scales of fluctuation (*SOFs*) on excavation-induced deformations. Probabilistic analyses are conducted on the basis of stochastic calculations to assess the failure of SS and RWD. The study can provide a reference in the field of reliability-based design braced excavations, with consideration of soil and structural failure.

2 Numerical Method for Modeling Braced Excavations

2.1 Plastic Hardening-Small-Strain Model

According to Puzrin et al. [33] and Burland et al. [34], the strain of soil in engineering works such as tunnels and braced excavations is mainly concentrated within a narrow range of values. Figure 1 provides the curves of soil stiffness decaying nonlinearly with increasing strain [35]. On a

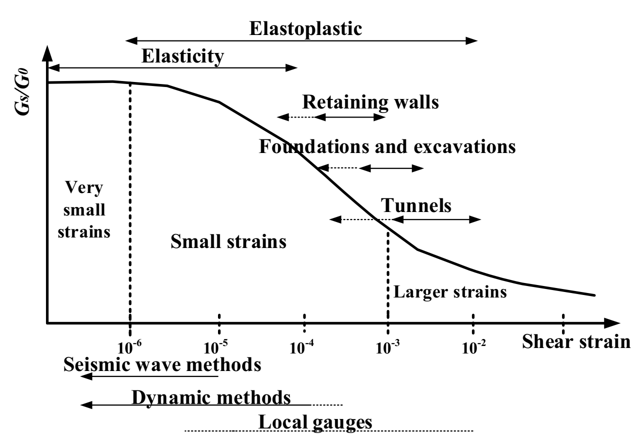

Fig. 1 Characteristic stiffness-strain behavior of soil with typical strain ranges for laboratory tests and structures [35]

logarithmic scale, stiffness reduction curves exhibit a characteristic S-shape; the small-strain behavior shall be considered in the study of soil and structure responses induced by excavation. In this regard, the small-strain characteristics have been considered in many studies of braced excavations [36–38]. Thus, the plastic hardening-small-strain model ('PH-SS model') is adopted to simulate the constitutive relationship of clay in this study. The PH-SS model is based on the hardening soil model, which can approximate the observed stress–strain behavior in clays, using Eq. (1):

$$\varepsilon_1 = \frac{1}{E_i} \cdot \frac{q}{1 - q/q_a} \tag{1}$$

where q_a denotes the asymptotic value of the deviatoric stress and E_i is the initial soil Young's modulus at a very low-strain ($< 10^{-6}$). To account for the small-strain characteristic, the initial or very small-strain shear modulus G_0 and the shear strain level $\gamma_{0.7}$ are additionally taken into account in FLAC^{3D} software [39]. The two parameters can be employed to address the small-strain stiffness via Eq. (2):

$$\frac{G}{G_0} = \frac{1}{\left(1 + 0.385 \cdot \left|\gamma/\gamma_{0.7}\right|\right)^2} \tag{2}$$

The soil parameters affect the excavation-induced deformation of soil. Hence, significant importance shall be attached to determining parameters of the PH-SS model. Previous research [40] was carried out to present a method of determination of parameters for clay layers based on laboratory tests. As an alternative, the empirical equations provided in the reference of FLAC^{3D} Version 6.0 [39] are used in this study, as shown by Eq. (3):

$$9 \cdot E_{oed}^{ref} = 9 \cdot E_{50}^{ref} = 3 \cdot E_{ur}^{ref} = G_0^{ref} \tag{3}$$

For simplicity, the paper conducts the studies in a single clay layer while ignoring the influence of soil layering. The clay parameters are listed in Table 2.

2.2 Numerical Model

Inspired by an example in the literature [39], a two-dimensional numerical model for the braced excavation is developed to study the SS and RWD. In reality, the numerical model is pseudo-two-dimensional with a size of 35 m (x axis) × 2 m (y axis) × 20 m (z axis). Figure 2 illustrates the geometry of the numerical model for braced excavations under plane-strain conditions. Due to the symmetry of the braced excavation cross section, only half of the excavation is used for modeling. The final depth of excavation is 6 m from the surface ($H = 6$ m) and its half-width is 7 m ($B = 7$ m). It is noted that the geometry of the model (35 m × 20 m) meets the requirements for minimizing the boundary effect according to the Saint-Venant principle. The diaphragm walls extends to 12 m depth and are braced at the top by horizontal struts at a 2-m interval. With reference to the technical specifications for a braced excavation, the vehicles and related personnel around the braced excavation are simplified to a uniform applied pressure of 20 kPa.

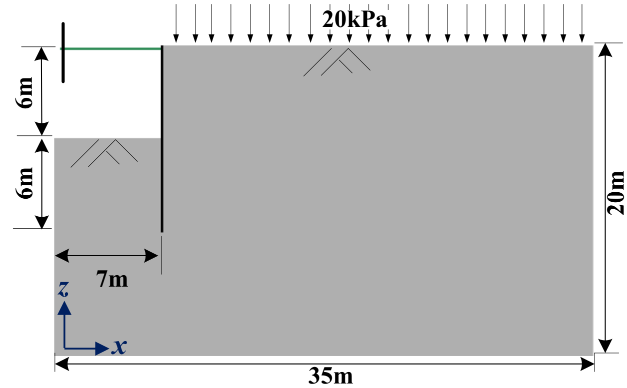

Fig. 2 Braced excavation model and its size

The PH-SS model is utilized to simulate the elastoplastic behavior of soil. Additionally, the soil is assumed to be completely without precipitation throughout the area to be excavated. In this regard, the area to be excavated is regarded as being in an undrained state.

The retaining system for a braced excavation typically consists of retaining walls and strut components. In this study, the liner element is used to simulate retaining wall, and the beam element is employed to represent structural components. Only the first support for braced excavation is considered in the numerical model. It is noted that the equivalent thickness of the wall is 0.51 m with its equivalent Young's modulus being 24 GPa. In addition, the equivalent modulus of internal support is set to 30 GPa. Tables 3 and 4 list the parameters of the retaining wall and internal support, respectively.

The average value of the shear strength for interface element between soil and wall is used here. Due to the spatial variability of soil properties, the stiffness of the adjacent soils varies with spatial position. In the code in FLAC^{3D}

Table 2 PH-SS model parameters: soft clay

Layer	γ/kN m^{-3}	φ'/°	c'/kPa	E_{50}^{ref}/MPa	E_{ur}^{ref}/MPa	E_{oed}^{ref}/MPa	υ	m	p^{ref}/kPa	G_0^{ref}/MPa	$\gamma_{0.7}$
Clay	17.0	20	13	4.5	13.5	4.5	0.35	0.9	100	40.5	2e^{-4}

Table 3 Retaining wall parameters

Attributes	Density/ kg m^{-3}	Young's modulus/ GPa	Poisson's ratio	Equivalent thickness/m
Values	2500	24	0.2	0.51

Table 4 Internal support parameters

Attributes	Density/ kg m^{-3}	Young's modulus/ GPa	Poisson's ratio	Cross-sectional area/m^2	Spacing/m
values	3000	30	0.2	1.0	2.0

[39], the normal stiffness K_n and the shear stiffness K_s can demonstrate the deformation performance of the interface element. If both stiffnesses are set too low, the interface element will be deformed too much and will penetrate the adjacent soils too much, rendering the simulation results unreasonable. If the values are high, it will cause difficulties in convergence. In this regard, the suggested values of interface stiffness are given as follows:

$$K_n = K_s = 10 \times \frac{K + \frac{4}{3}G}{\Delta z} \tag{4}$$

where $K+4G/3$ represents the compression stiffness, K and G denote the average values of the soil bulk stiffness and shear stiffness, respectively. Δz is the element size on the low-stiffness side among the adjacent soil elements.

In this study, the excavations are conducted as follows:

Step 1. Generate the initial stresses in a convergent state;
Step 2. Activate the liner element;
Step 3. Excavate the soil of the braced excavation to 2 m below the surface;
Step 4. Activate the beam element;
Step 5. Continue to excavate the soil to 6 m below the surface.

Figure 3 shows the results of RWD and SS induced by braced excavation in a deterministic framework. For the RWD, it appears convex. The maximum value of RWD is −26.25 mm, about 0.44% of the excavation depth. It is noted that the maximum RWD occurs around the base. Meanwhile, the maximum SS is located 4.5 m away from the wall. The maximum SS is −15.29 mm, about 0.26% of the excavation depth. Based on the calculated results, the ratio between the maximum RWD and SS is 1.72. Additionally, the settlement value extends to the side away from the retaining wall and gradually tends to be stable, while the settlement of soil close to wall is relatively large due to the weight of the retaining wall.

3 Random Finite Difference Method

3.1 Generation of Random Field in Clays

The inherent spatial soil variability is one of the main sources of uncertainty in geotechnical problems because of depositional and post-depositional processes. With an attempt to address the spatial variability of soil properties, Vanmarcke [8] proposed a method of establishing random fields. One of the effective approaches to generating a random field is taking the prescribed auto-correlation functions (ACFs) into account using the covariance matrix decomposition method (CMDM) [41]. The method is employed for its simple implementation and high accuracy for a small simulated domain, making it suitable for excavation-induced deformation, herein. In this regard, the CMDM is used in this paper.

In the implementation of CMDM, the mean, coefficient of variation (*COV*), and *SOF* of the soil parameters shall

Fig. 3 Deformation induced by braced excavation in a deterministic framework

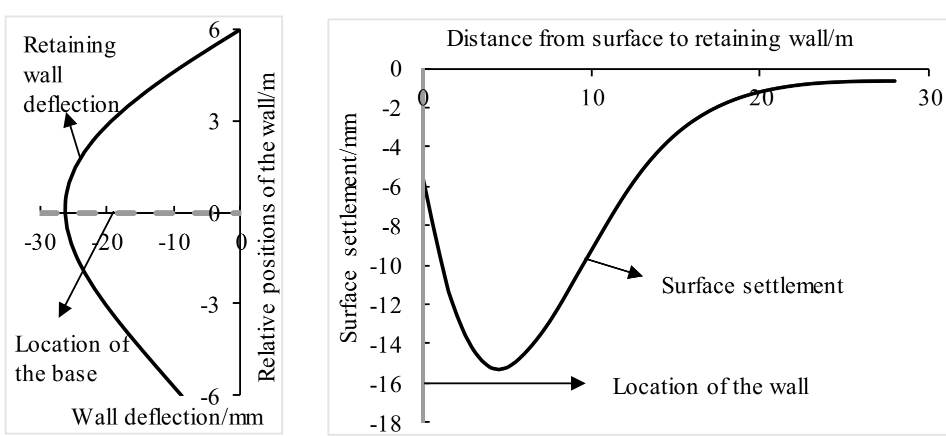

be firstly specified for characterizing a random field. The stationary random field is generated to simulate a homogeneous soil layer in this paper. Meanwhile, the lognormal Gauss random field is utilized to describe the soil parameter spatial variability for its nonnegativity. To determine the spatial correlation of geotechnical parameters in both vertical and horizontal directions, an anisotropic random field identified by exponential auto-correlation function (ACF) is used, associating with the horizontal and vertical *SOFs*. Studies [18, 20] found that the parameters of natural soils are spatially anisotropic due to their geological deposition processes, illustrating that the horizontal *SOF* is generally 10–80 m, and the vertical *SOF* is 1–3 m. The anisotropic coefficient ξ is used to describe the transversely isotropic correlation framework.

A uniform clay layer is discretized into $m \times n$ quadrilateral elements. Figure 4 depicts the discretization for random fields, where m and n denote the number of elements in each direction, respectively, and (x_i, z_j) denotes the coordinates of the centroid of each element, $i = 1, 2, \ldots, m$, $j = 1, 2, \ldots, n$. The single exponential ACF is used to elucidate the correlation between different points in clay, as follows:

$$\rho(\tau_x, \tau_z) = \exp\left[-2 \times \left(\frac{|\tau_x|}{\theta_x} + \frac{|\tau_z|}{\theta_z}\right)\right] \tag{5}$$

where τ_x and τ_z represent the absolute distance between any two spatial points in horizontal and vertical directions, respectively, and θ_x and θ_z denote the horizontal and vertical *SOFs*. Then, the auto-correlation coefficient can be calculated using Eq. (5), and the auto-correlation matrix $C_{n\times n}$ is written as follows:

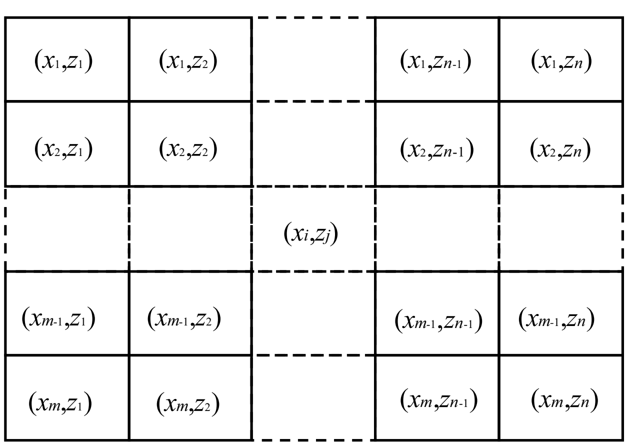

Fig. 4 Discretization for random fields

$$C_{n\times n} = \begin{bmatrix} 1 & \rho(1,2) & \cdots & \rho(1,n) \\ \rho(2,1) & 1 & \cdots & \rho(2,n) \\ \vdots & \vdots & \ddots & \vdots \\ \rho(n,1) & \rho(n,2) & \cdots & 1 \end{bmatrix} \tag{6}$$

where ρ represents the auto-correlation coefficient between any two centroid points.

Since $C_{n\times n}$ is a positive definite symmetric matrix, the Cholesky decomposition technique is used to decompose $C_{n\times n}$ into the product of a lower triangular matrix L and its corresponding transpose:

$$C_{n\times n} = L \cdot L^T \tag{7}$$

where L^T denotes the transpose of the matrix L. Then, a realization of the auto-correlated standard Gaussian random field can be deduced according to:

$$Z = L \cdot Y \tag{8}$$

where Y is a vector randomly generated. Using the regenerated Y, the Gaussian random field can be derived.

To incorporate the random field model into numerical model, the finite difference code FLAC^{3D} is used herein. With the built-in FISH language, FLAC^{3D} can identify the positions of the discretized elements according to the proximity principle between numerical elements and random field coordinates, thereby realizing the mapping of an independently generated random field model to the numerical model.

In this paper, $E_{\text{oed}}^{\text{ref}}$ is considered as a spatially variable parameter. On the basis of Eq. (3), other stiffness parameters are derived to indicate the corresponding stiffness random field.

3.2 Calculation of the Probability of Failure

Since random fields are used to describe the spatial variability of soil parameters, the responses of excavation-induced deformation can become stochastic. In this paper, MCS is adopted to generate N_s realizations of random fields for stochastic calculation and to perform a subsequent reliability analysis of structure and soil responses. To cope with such stochastic problems, the probability of failure (P_f) is employed to express the possibility of excavation-induced deformation. The method of calculating P_f can be expressed as follows:

$$P_f = P[Z < 0] = \frac{1}{N}\sum_{i=1}^{N} I[Z < 0] \tag{9}$$

$$Z = S_{\text{sto}} - S_{\text{lim}} \tag{10}$$

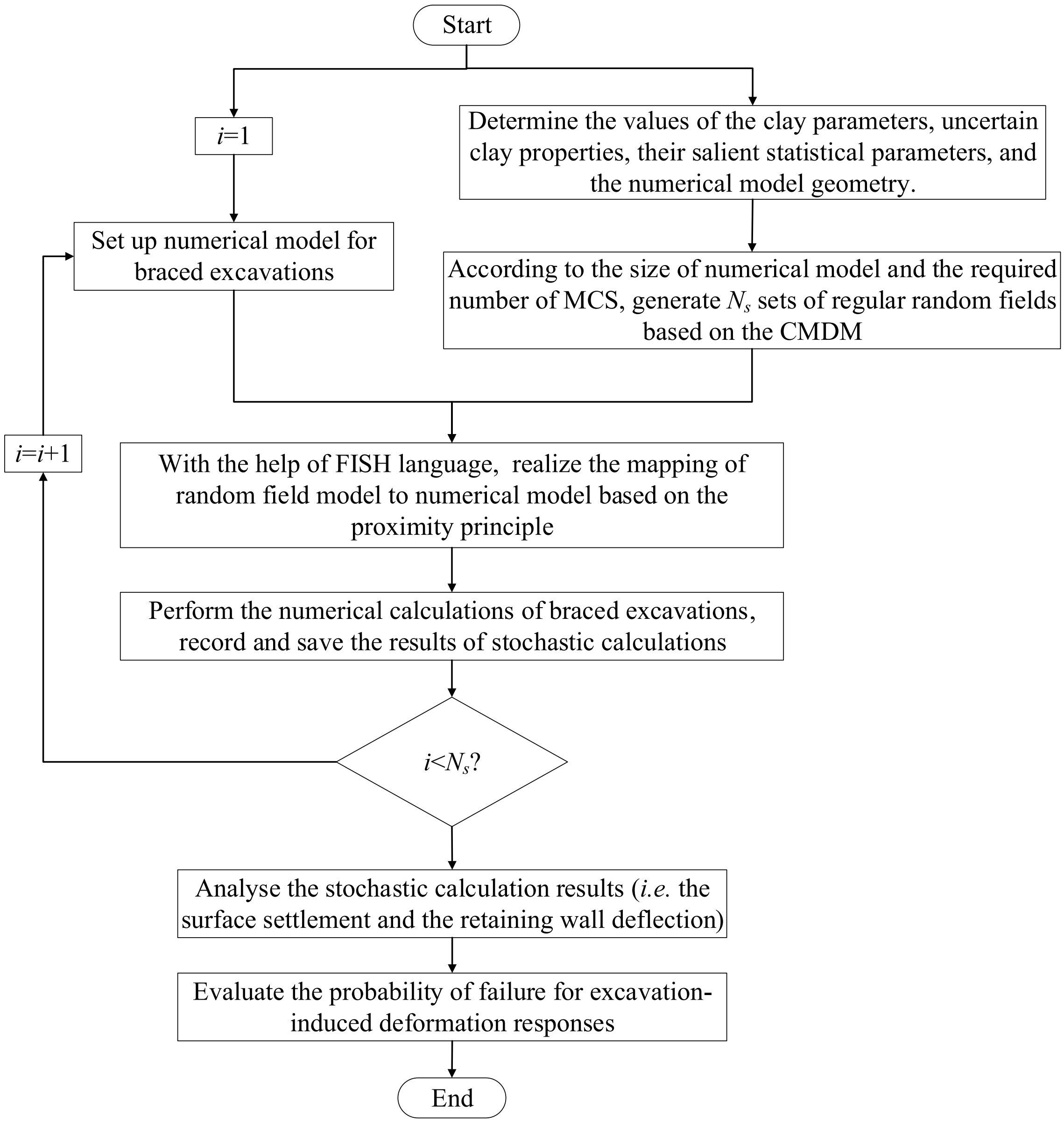

Fig. 5 Flowchart through of MCS for excavation-induced responses

where Z is the serviceability limit state function (LSF), in which S_{sto} is the response of stochastic calculation and S_{lim} refers to the limiting value of the corresponding response, N denotes the number of MCS, and $I[-]$ represents the indicator function. When $Z < 0$, $I[-]$ is 1, otherwise zero.

3.3 Implementation Procedure of RFDM for Reliability Analysis

Here, random field theory and numerical analysis are combined to investigate the influences of clay property spatial variability on the responses of soil and structure deformation induced by excavation. Based on the aforementioned introduction of the proposed methods, i.e., RFDM, more details of the implementation procedure are outlined as below:

Step 1: Determine the values of the clay parameters, uncertain clay properties, their salient statistical parameters, and the numerical model geometry.
Step 2: Discretize the numerical model, and generate a random field model in the same size of the corresponding numerical model.
Step 3: Perform N_s MCS to obtain different stochastic results, including the values of RWD and SS.

Table 5 Calculated cases of stochastic analyses

Case name	Variable	Parameter distribution and ACF	*COVs*	*SOFs*		
				θ_x	θ_z	ξ
MCS-z1	θ_z	Lognormal distribution, exponential (SExp)	0.3	4.8*H*	2.4*H*	2
MCS-z2					1.2*H*	4
MCS-z3					0.6*H*	8
MCS-z4					0.3*H*	16
MCS-z5					0.15*H*	32
MCS-z6					0.075*H*	64
MCS-×1	θ_x	Lognormal distribution, exponential (SExp)	0.3	0.6*H*	0.3*H*	2
MCS-×2				1.2*H*		4
MCS-×3				2.4*H*		8
MCS-×4				4.8*H*		16
MCS-×5				9.6*H*		32
MCS-×6				19.2*H*		64
MCS-v1	*COV*	Lognormal distribution, exponential (SExp)	0.1	4.8*H*	0.3*H*	16
MCS-v2			0.2			
MCS-v3			0.3			
MCS-v4			0.4			
MCS-v5			0.5			

The excavation depth *H* is 6 m. ξ represents the anisotropy coefficient, $\xi = \theta_x/\theta_z$

Step 4: Discuss the influences of *SOFs* and *COVs* of soil stiffness on the RWD and SS, then investigate the probability of failure of excavation-induced deformations.

Figure 5 shows the flowchart for excavation-induced deformation assessment using the RFDM.

4 Stochastic Analysis for the Braced Excavation

In this section, stochastic responses for SS and RWD induced by excavations are illustrated. A series of anisotropic random fields ($\theta_x \neq \theta_z$) are generated to identify the influences of both the *COVs* and the *SOFs* on the excavation-induced responses.

Based on the literature [18, 20], the horizontal and vertical *SOFs* of soil stiffness lie in the range of 10–80 m and 1–3 m, respectively. In this regard, this subsection evaluates the responses caused by excavation for the baseline case in the conditions of $\theta_x = 4.8H = 28.8$ m, $\theta_z = 0.3H = 1.8$ m, and $COV = 0.3$. To assess the effects of *COVs* and *SOFs* on the responses, a series of cases are investigated under different combinations of *COVs* and *SOFs* (Table 5).

Before conducting MCS, the number of simulations is determined. Figure 6 shows the means and *COVs* of maximum deformations (i.e., SS and RWD, the same below) with the numbers of simulations. It can be found that the means and *COVs* of both maximum SS and maximum RWD tend to be stable when N_s reaches 1000; thus, $N_s = 1000$ is adopted here.

4.1 Influences of SOFs on Excavation-Induced Deformation Responses

In this subsection, *SOFs* are paid enough attention in the field of deformations influenced by spatial variability of soil parameters. It is noted that both horizontal and vertical *SOFs* arise in engineering practice; thus, both *SOFs* are considered here. For excavation-induced responses, a series of cases, named MCS-z1 to MCS-z6, are analyzed to identify the influences of vertical *SOFs* while the cases (MCS-x1 to MCS-x6) are analyzed to study the effects of horizontal *SOFs*.

Figure 7 shows the stochastic results corresponding to cases MCS-z1, MCS-z4, and MCS-z6. For better comparison, the deterministic results are also shown with the black line while the stochastic results are denoted by the gray line. As shown in Fig. 7, the stochastic results exhibit a trend of aggregation with an increase in the values of ξ (corresponding to the decrease of vertical *SOFs*); however, the *SOFs* exert no influence on the shape of the deformation curve. The stochastic calculated results fluctuate around the solutions obtained by deterministic calculation. Overall, the stochastic results in majority are larger than those obtained in the deterministic scenario, which is mainly due to the dominant effects of low stiffness and the asymmetry of the logarithmic random distribution of stiffness. It is noted that

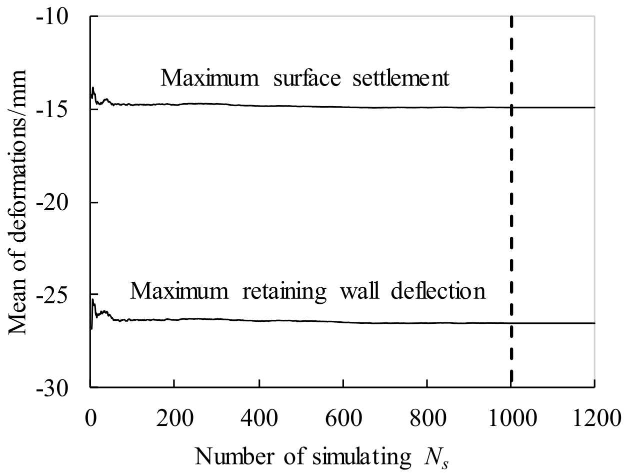

(a) Mean of maximum deformation

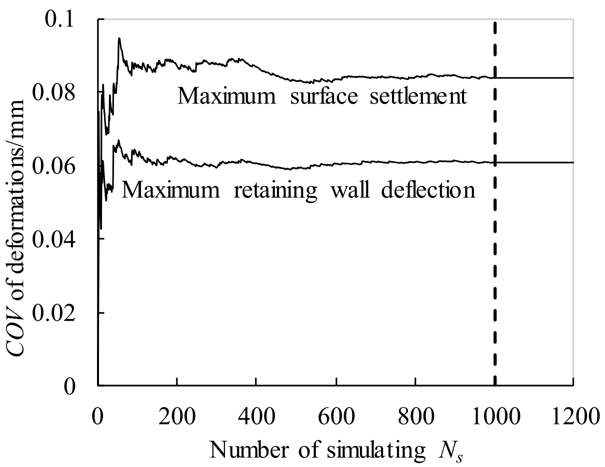

(b) *COV* of maximum deformation

Fig. 6 Mean and *COV* of maximum deformation

the stochastic results in the analysis of cases MCS-z1 to MCS-z6 are similar to those obtained when analyzing cases MCS-x1 to MCS-x6. Meanwhile, the stochastic results are more influenced by vertical *SOFs* than by horizontal *SOFs*.

Based on the Monte Carlo method, 1000 simulations have been conducted for all cases. It can be observed from Fig. 7 that the maximum deformations obtained by any stochastic calculation are different. In this regard, statistical analysis is conducted to identify the effects of *SOFs* on the excavation-induced maximum deformations. Figure 8 shows the influences of *SOFs* on the mean values and *COVs* of maximum deformations. Mean values of both the SS and the RWD are less affected by the *SOFs* of the soil stiffness, which indicates the maximum deformations are generally the same in the 'average sense' of the influences of *SOFs*. Further to investigate the 'average sense' of the maximum deformation, the entire 1000 simulations are analyzed here. It is assumed that both the soil stiffness and maximum deformation follow the lognormal distribution. For the lognormal distribution ($Y = \ln X - N(\mu_{ln}, {\sigma_{ln}}^2)$), its characteristic values and those of the normal distribution can be mutually inter-converted (Table 6).

For soil stiffness E, $\ln E$ follows a normal distribution with mean and standard deviation given by:

$$\begin{aligned} \sigma_{\ln}^2 &= \ln(1 + \sigma^2/\mu^2) \\ \mu_{\ln} &= \ln(\mu) - \tfrac{1}{2}\sigma_{\ln}^2 \end{aligned} \qquad (11)$$

According to the literature [9], since the soil stiffness follows a lognormal distribution, the probability that the stiffness is less than the average value of stiffness is greater than 50% in random field model of the soil stiffness. It is recommended that engineers use the geometric mean stiffness as the equivalent characteristic stiffness. It can be seen from Table 6 that the average soil stiffness is greater than its geometric mean; thus, the results obtained by using the average value of soil stiffness are lower than the results using the geometric mean. The expression of geometric mean shows it is independent of the *SOF*, but is related to the standard deviation (or *COV*), which further explains the conclusion that the mean of the maximum deformations is independent of the *SOF*.

For the *COVs* of maximum deformations in Fig. 8b, they show a tendency to increase as the *SOFs* (horizontal and vertical) increase. The influences of vertical *SOFs* on the *COVs* of maximum deformations are found to be greater than those of horizontal *SOFs*. When the vertical *SOFs* lie in the range of 0.6H to 2.4H, the *COV* of SS shows a relatively smooth trend with the anisotropy coefficient ξ while that of RWD does not show any abnormalities, as defined by the correlation of vertical *SOF*. When the vertical *SOFs* are close to the size of the excavation, the probability that high-stiffness regions and low-stiffness regions occur in the excavation area increases, making the excavation-induced response more broadly scattered. It is noted that the influences of vertical *SOFs* on SS and RWD are differently, perhaps as a result of the difference in stiffness between the soil and the wall.

Figure 9 shows the location of maximum deformation considering different *SOFs*. It is observed that the location of maximum SS mainly lies in the range of 0.8H to 0.9H with those of RWD around the base. Meanwhile, with increasing anisotropy coefficient ξ (the decrease of vertical *SOFs*), the scatter degree of maximum SS and its location first decreases, then increases. In the case of *SOF* corresponding to the size of the excavation, the scatter of SS is the greatest, consistent with the correlation of vertical *SOF*. For the RWD, its location becomes more concentrated with increasing anisotropy coefficient ξ, which is

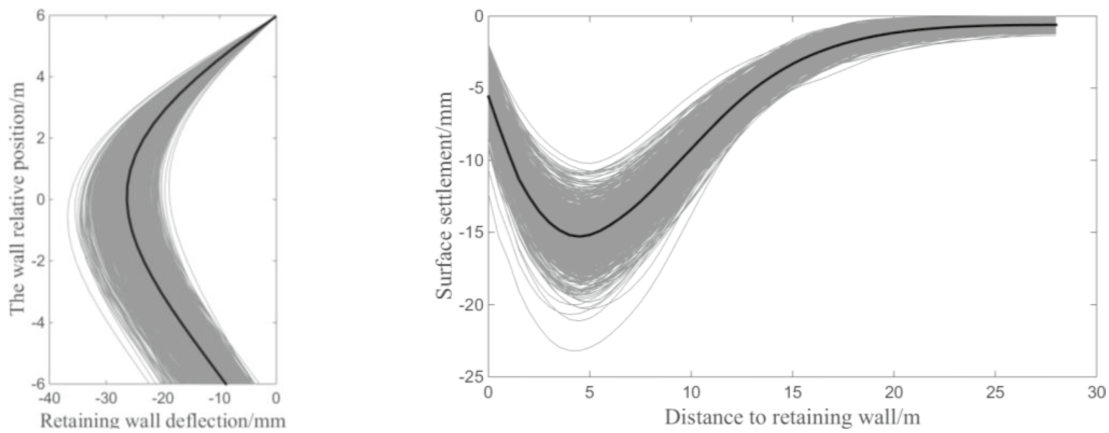

(a) MCS-z1

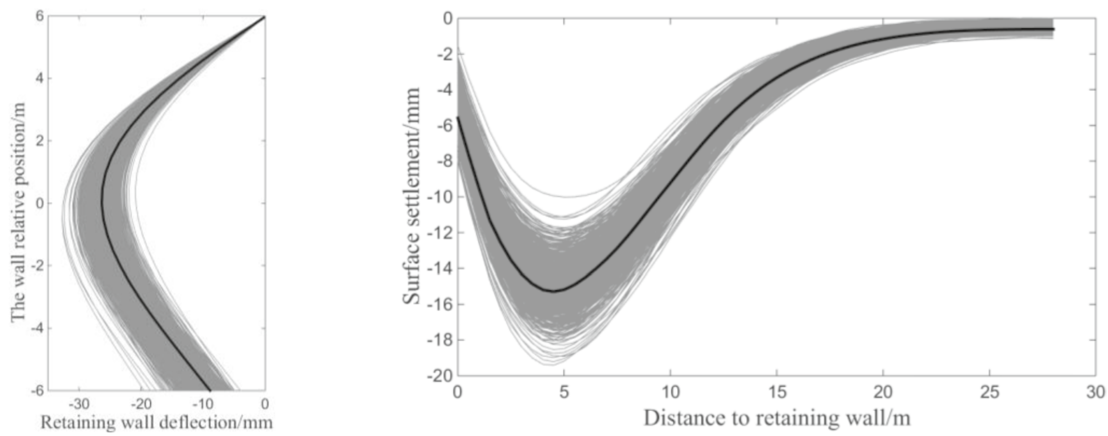

(b) MCS-z4

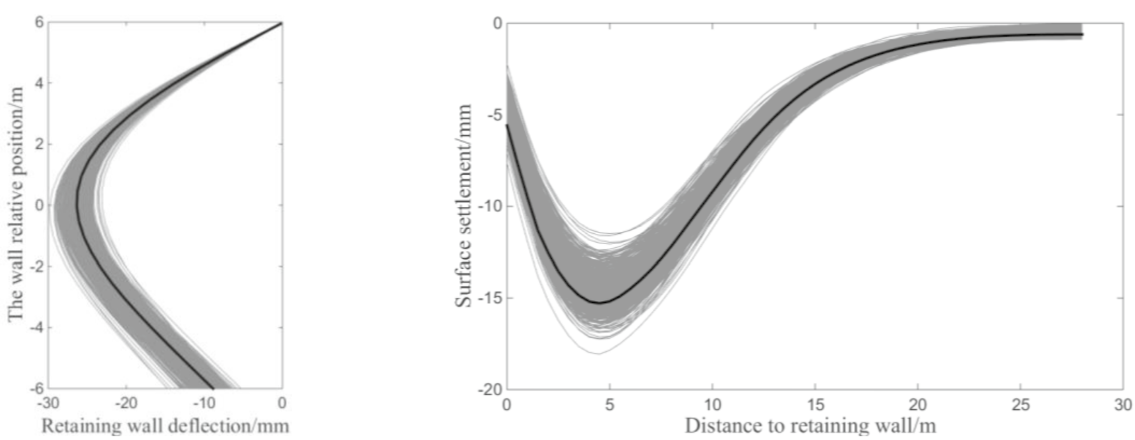

(c) MCS-z6

Fig. 7 Retaining wall deflection and surface settlement under different *SOFs*

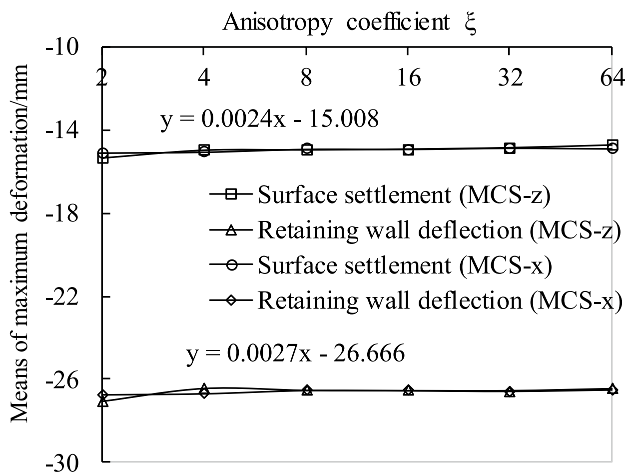

(a) The means of maximumdeformations

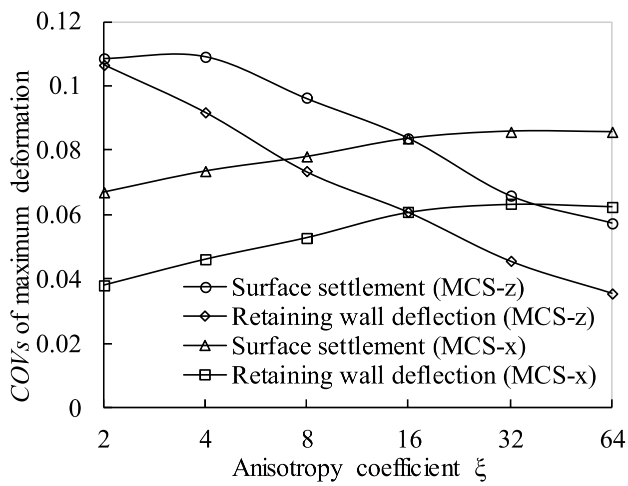

(b) The *COVs* of maximum deformations

Fig. 8 Effects of *SOF* on the means and *COVs* of maximum deformations

Table 6 Characteristic values of the lognormal distribution

Average value (arithmetic mean)	Median	Common value	Geometric mean
$\exp(\mu_{\ln}+\sigma_{\ln}{}^2/2)$	$\exp(\mu_{\ln})$	$\exp(\mu_{\ln}-\sigma_{\ln}{}^2)$	$\exp(\mu_{\ln})$

different from the influence on SS. This may be due to the difference in stiffness between the soil and the wall. Based on the locus of maximum RWD (Fig. 9b), two modes of RWD are presented in this subsection, as shown in Fig. 10.

Mode 1: The location of maximum RWD is above the base, as shown in Fig. 10a. Due to the inhomogeneity of strong regions and weak regions, different loci of maximum RWD may occur. The weak region occurs above the base and the base below tends to be stronger, making it difficult to transfer displacement to the base below.

Mode 2: The location of maximum RWD lies below the base, as shown in Fig. 10b. The strong region of unloading stiffness lies above the base while the weak region is below the base. In this regard, more deformation is assigned to the area below the wall.

Figure 11 shows the variations of the ratios between maximum SS (δ_{vm}/H) and maximum RWD (δ_{hm}/H) for different *SOFs*, corresponding to MCS-z1, MCS-z4, and MCS-z6. It shall be shown that the maximum SS (δ_{vm}/H) and the maximum RWD (δ_{hm}/H) are dimensionless. This study uses a range angle α to describe the degree of scatter of the ratios between δ_{vm}/H and δ_{hm}/H. In all the cases, the ratios between δ_{vm}/H and δ_{hm}/H are distributed within a particular range. As an example, α is 13.74°, 10.90°, and 9.95° at $\xi=2$, 16, and 64, respectively. With increasing ξ, the vertical *SOFs* decrease, the range angle α decreases, and the average ratios between the two deformations (δ_{vm}/H and δ_{hm}/H) tend to increase. This may be explained by the fact that more soil displacement will be assigned to surface settlement instead of horizontal displacement for such a braced excavation in variable clays. Compared to the deterministic result (1.72), the ratios between δ_{vm}/H and δ_{hm}/H calculated in a stochastic framework vary widely, with a bigger value in the 'average sense'. This may result from the inhomogeneity of strong regions and weak regions and it indicates that the ratios between δ_{vm}/H and δ_{hm}/H will be underestimated if the spatial variability of soil properties is not considered.

As illustrated, the deformed curves may be stochastic due to the inhomogeneity of soil stiffness. In this regard, four modes corresponding to different combinations of SS and RWD are proposed by comparing data with the deterministic results. It is noted that the most scattered results may be obtained in the case when *SOF* corresponds to the size of the excavation. Thus, scenario MCS-z2 is taken as an example to illustrate the modes of deformation of SS and RWD. Figure 12 shows four modes of SS and RWD by comparing the data with deterministic results. Mode 1 indicates that the SS and RWD are both more deformed than their deterministic results. This can be explained that the weak region of soil stiffness is widely distributed in the area around the excavation, increasing the values of SS and RWD. Mode 2 represents a larger SS and a smaller RWD while the opposite results arise in Mode 3, which results from the inconsistent distribution of weak regions and strong regions (or intermediate regions) on the two sides of the retaining wall. Mode 4 denotes the scenario wherein smaller values of SS and RWD are obtained in the stochastic calculation when strong regions are located around the excavated areas. In general, the inhomogeneity of strong regions and weak regions leads to different modes for SS and RWD.

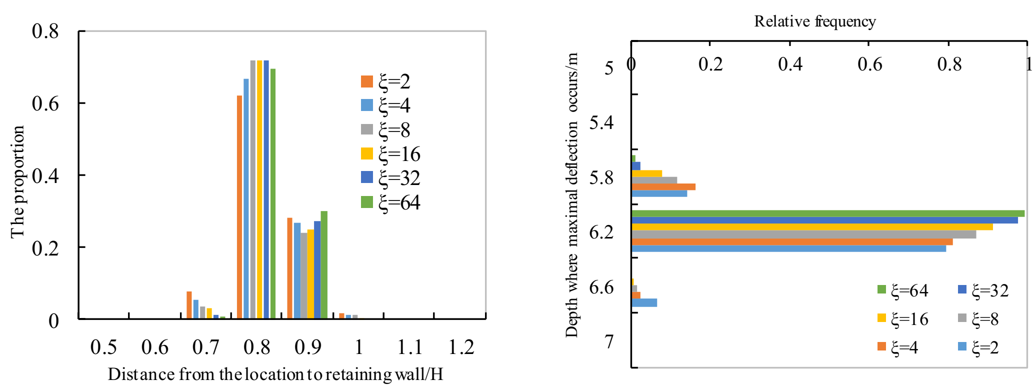

(a) Surface settlement **(b)** Retaining wall deflection

Fig. 9 Location of maximum deformation

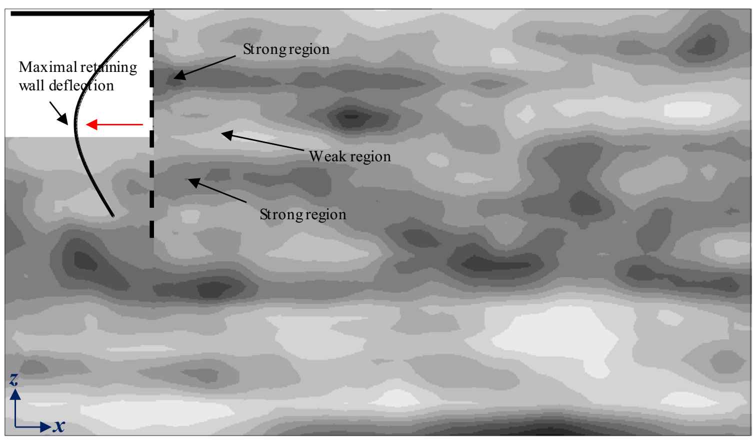

(a) Mode 1 corresponding to the case in which the maximum RWD occurs above the base

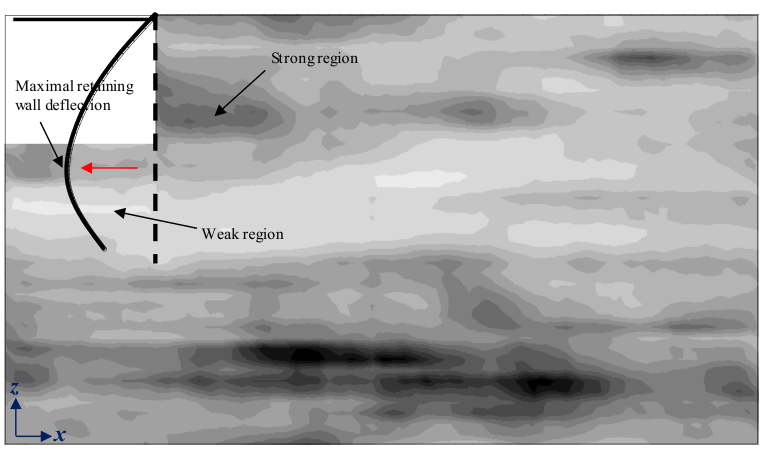

(b) Mode 2 corresponding to the case in which the maximum RWD occurs below the base

Fig. 10 Two modes of RWD with consideration of its location

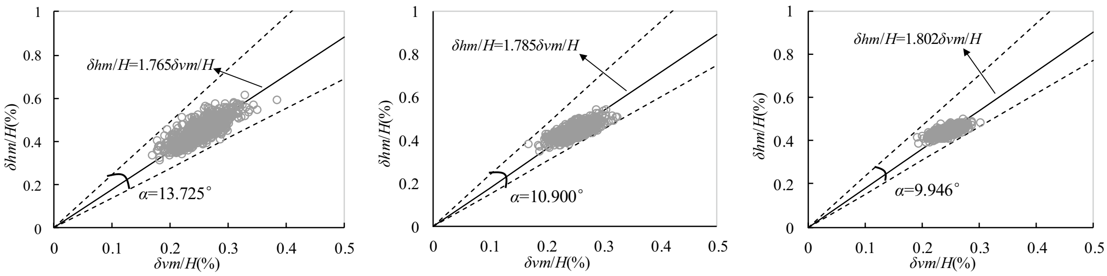

(a) MCS-z1 (ξ = 2) **(b)** MCS-z4 (ξ = 16) **(c)** MCS-z6 (ξ = 64)

Fig. 11 Relationship between maximum SS and maximum RWD

4.2 Influences of COVs on Excavation-Induced Deformation Responses

As can be imagined from engineering experience, the *COV* of soil stiffness will affect the characterization of soil spatial variability, which subsequently influences the excavation-induced responses. A series of cases, as shown in Table 5 (from MCS-v1 to MCS-v5), are analyzed to study the corresponding influence.

Figure 13 shows the calculated results when $COV=0.1$, 0.3, and 0.5, corresponding to MCS-v1, MCS-v3, and MCS-v5, respectively. It is noted that three cases of $COV=0.1$, 0.3, and 0.5 indicate three levels of soil stiffness variability (low, moderate, and high). As the *COV* increases, the degree of scatter of curves increases accordingly, whether they are plots of SS or RWD. However, the shape of the curve does not vary with the variation of *COV*, which is consistent with the result obtained in the study of ξ. These conclusions might result from the soil spatial correlation, indicating the distributions of low-stiffness areas and high-stiffness areas. The correlation of soil stiffness shows a decreasing trend with an increase in *COVs*.

Figure 14 illustrates the influences of *COVs* on the mean values and *COVs* of maximum deformations. The results associated with the mean values of maximum deformation are opposite thereto: the surface settlement increases slightly while the results for the retaining wall show a slight decreasing trend with increasing *COV*. This is in line with the aforementioned conclusion. From the expression of geometric mean given in Table 6, it is noted that this value is independent of the *SOF* of the stiffness, only the standard deviation (or *COV*) thereof. For the *COVs* of maximum deformation in Fig. 14b, both results increase in a quasi-linear manner with an increase in soil stiffness *COV*.

Figure 15 shows the location of maximum deformation in different cases. The location of maximum SS occurs in the range of 0.6–0.8H while that of maximum RWD is distributed around the base. With the increase of *COVs*, the location of maximum SS broadens. The same conclusion is manifest for the maximum values of RWD.

Figure 16 describes the relationship between the maximum SS and the maximum RWD in different cases with the variations of *COVs*. As shown in the aforementioned study, some similar conclusions can be drawn with regard to the influences of *COVs* on these ratios. An increasing trend in angle α, corresponding to the increase of its degree of scatter, can be found as the *COV* increases. For a given *SOF*, the average ratios between δ_{vm}/H and δ_{hm}/H are found to increase as the *COV* increases. It is noted that the influence of ξ (or *SOFs*) is more moderate, compared to the effects of *COVs*. In addition, similar to the study on the influences of *SOFs*, the ratios between δ_{vm}/H and δ_{hm}/H will also be underestimated if the spatial variability of soil properties is ignored.

5 Probability Analysis for Deformations Induced by Excavation

In the stochastic calculations, the deformation results for the surface and retaining wall obtained from each MCS are different. Thus, it is necessary to study the characteristics of SS and RWD caused by excavation using probabilistic analysis.

The baseline case ($COV=0.3$, $\theta_x=4.8H=28.8$ m, $\theta_z=0.3H=1.8$ m) is selected for reliability analysis. Meanwhile, based on the baseline case, three groups of cases (MCS-z, MCS-x, and MCS-v) are analyzed to study the influences of vertical *SOFs*, horizontal *SOFs*, and *COVs* on the excavation-induced stochastic responses.

Figure 17 shows the frequency histogram of maximum values of the deformations and their cumulative distribution functions in the baseline case. By observing the results, the average value of maximum SS is − 14.92 mm while the mean of the maximum RWD is − 26.56 mm. It is noted that the average maximum SS is slightly less than

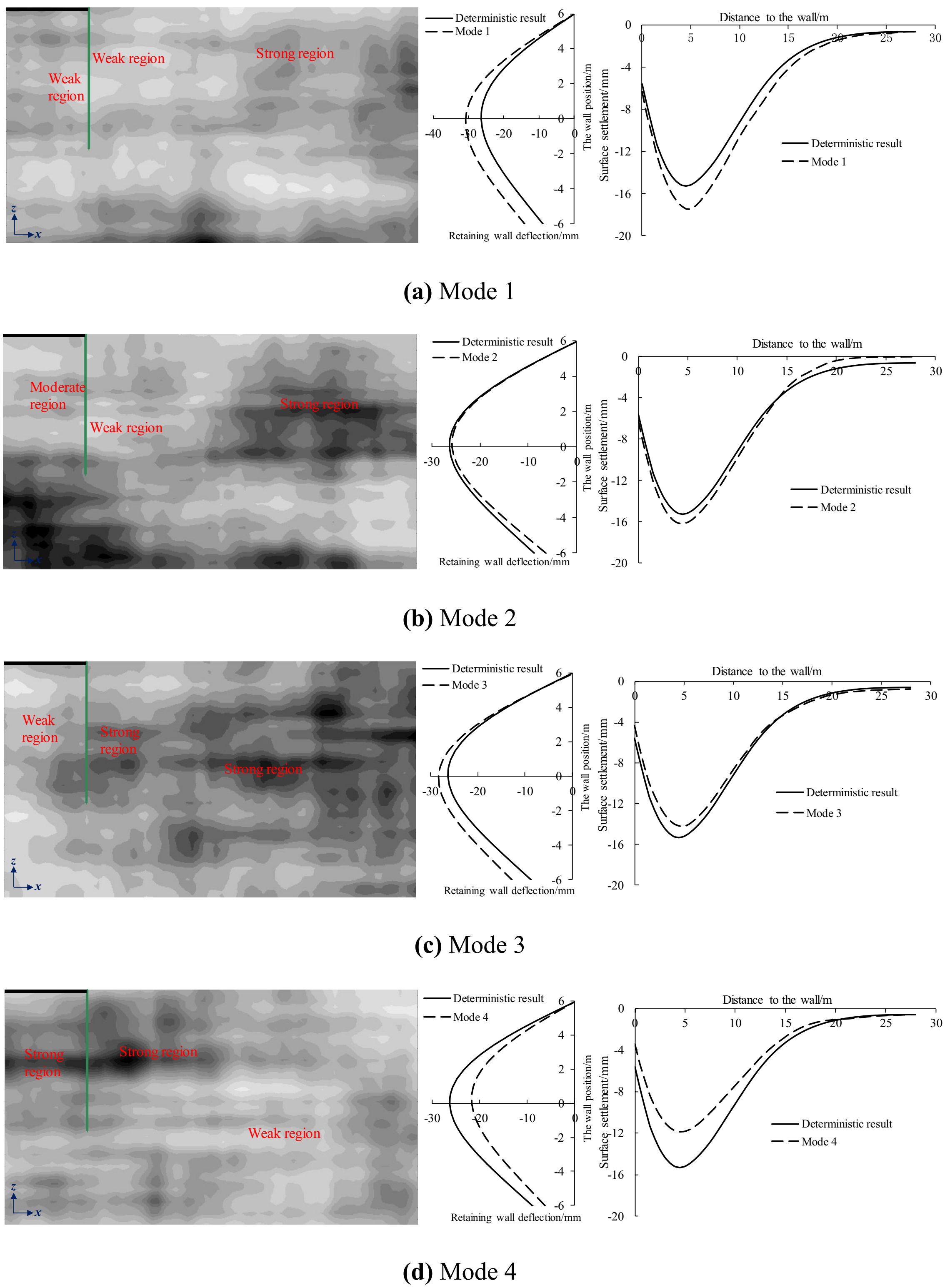

Fig. 12 Four modes of SS and RWD compared with the deterministic results

the corresponding deterministic result (− 15.29 mm) while the average maximum RWD is slightly larger than that in the deterministic calculation (− 26.25 mm). This may be explained by the inhomogeneous distribution of the soil strength, especially in zones of weakness [9, 42]. With the influence of the weak region, soil is more assigned to the direction of the retaining wall in its displacement field, increasing the value of RWD.

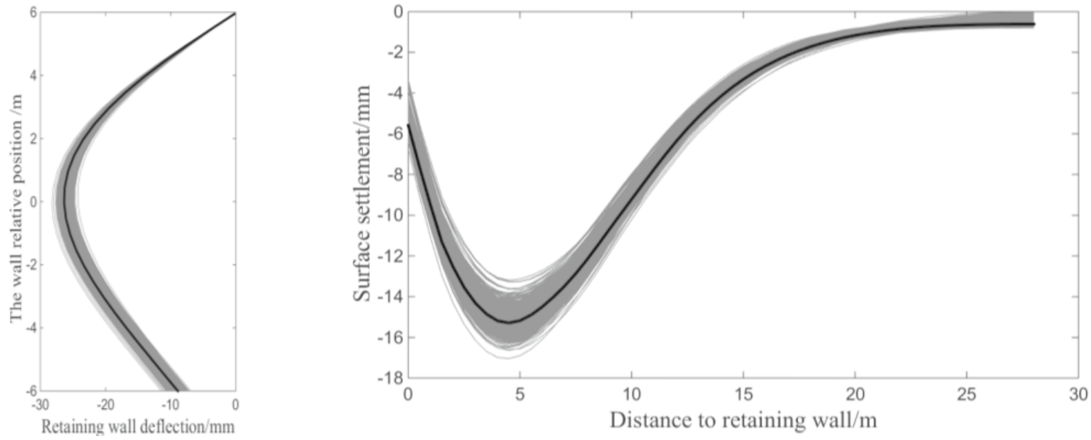

(a) MCS-v1

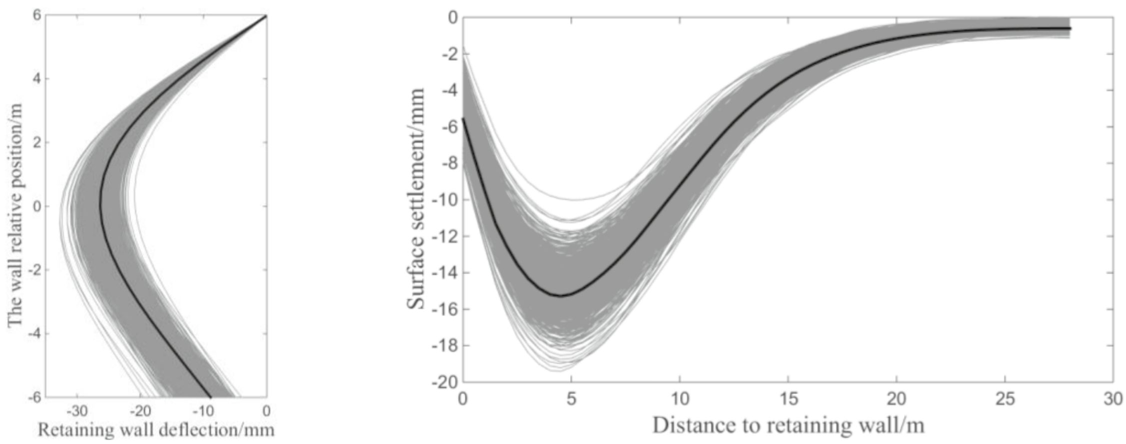

(b) MCS-v3

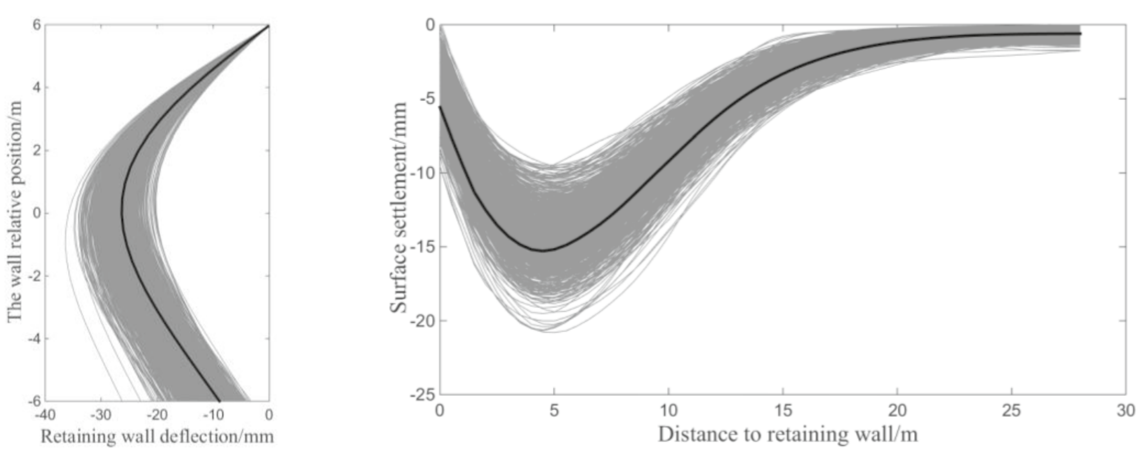

(c) MCS-v5

Fig. 13 RWD and SS under different *COVs* ($\xi = 16$, $\theta_x = 4.8H$, $\theta_z = 0.3H$)

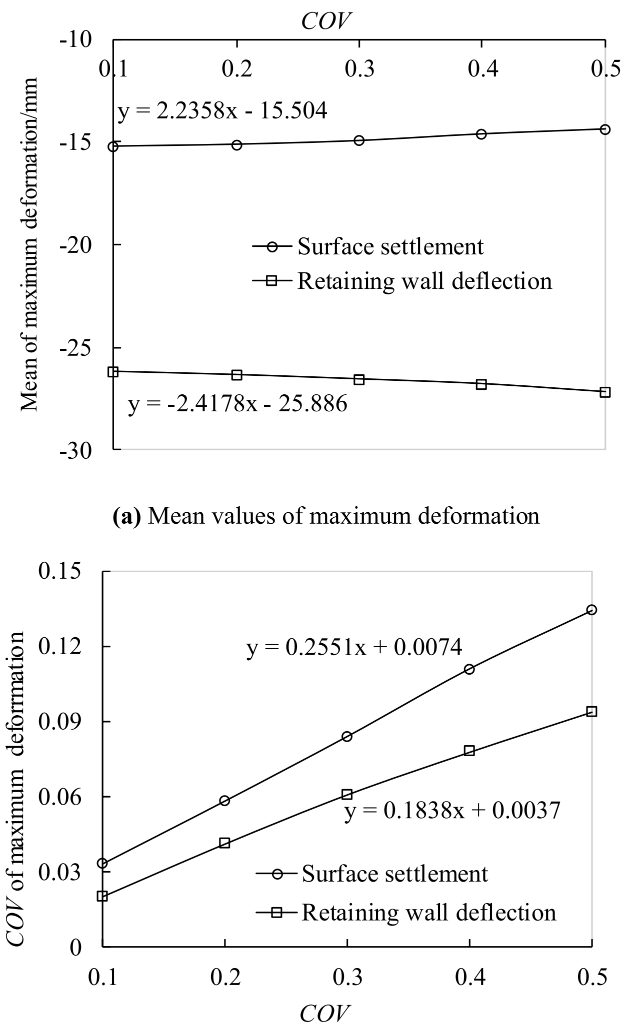

(a) Mean values of maximum deformation

(b) *COVs* of maximum deformation

Fig. 14 Effects of the *COVs* of stiffness on the *COVs* and mean values of maximum deformation

It is acknowledged that risks of excessive deformation may occur during the construction of braced excavation. Thus, it is necessary to determine safe limiting values of excavation-induced deformation. This study performs probability analyses of the maximum deformations based on 1000 runs of the MCSs. As provided in Eqs. (9) and (10), P_f and LSF are used to address the problem. Figure 18 compares the probability of failure estimated at a series of limiting deformations (i.e., SS and RWD) at various combinations of *COVs* and *SOFs*. For Fig. 18a, b, this section just shows the solutions resulting from variations in vertical *SOFs*. Overall, the probability of failure by excessive deformation can be overestimated or underestimated when ignoring the spatial variability of soil properties. Additionally, it is found that P_f decreases with the limiting SS or RWD at different combinations of *COVs* and *SOFs* (or ξ). Nevertheless, *COVs* and *SOFs* can dominate the rate of decrease of P_f. As the *SOFs* increase (ξ decreases), the maximum deformations vary more widely, and the probability of exceeding limiting values increases accordingly. In this regard, a similar conclusion can be obtained with an increase in *COVs*.

Figure 18 provides a beneficial reference for an assessment of maximum SS or maximum RWD before the construction of a braced excavation.

6 Conclusion

This study presents the effects of spatial variability of soil stiffness on the braced excavation in clays using the RFDM. Attention is mainly paid to *SOFs* (including horizontal and vertical variations thereof) and *COVs* when illustrating the spatial variability. The spatial variability of soil properties is modeled in the framework of random field theory using a series of combinations of *SOFs* and *COVs*. On the basis of

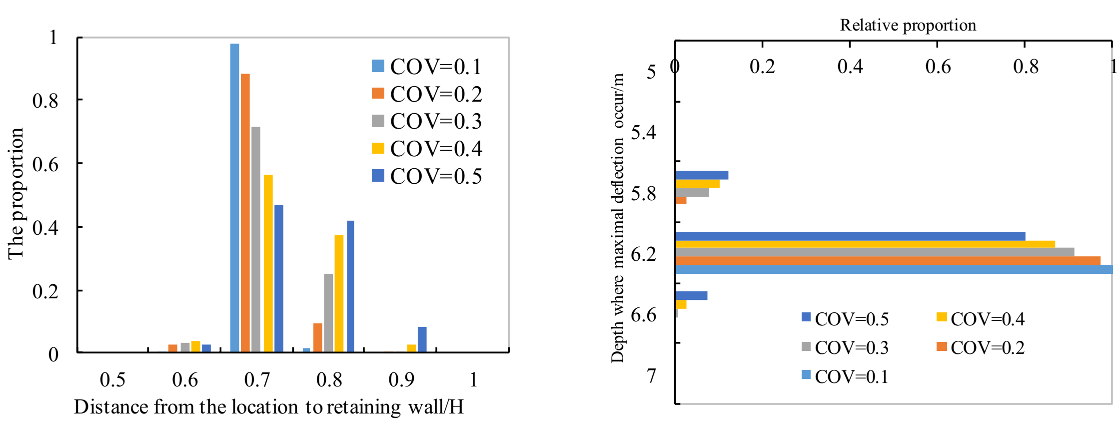

(a) Surface settlement **(b)** Retaining wall deflection

Fig. 15 Location of maximum deformation

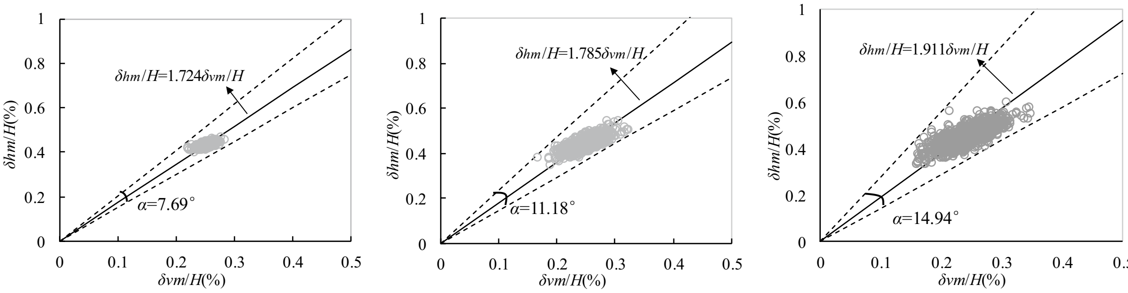

(a) $COV = 0.1$ **(b)** $COV = 0.3$ **(c)** $COV = 0.5$

Fig. 16 Relationship between maximum SS and maximum RWD

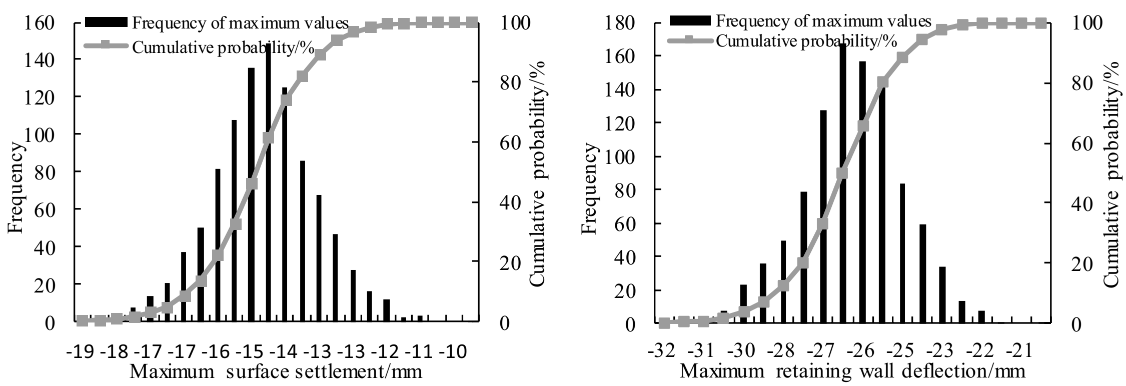

(a) Maximum surface settlement **(b)** Maximum retaining wall deflection

Fig. 17 Histogram of maximum deformations induced by excavation

the results presented in this study, several conclusions are drawn and summarized as follows:

1. Combining the small-strain characteristics of the soil and the spatial variability of soil properties, an algorithm is developed to facilitate the FDM-based probabilistic assessment in the framework of MCS.
2. The effects of weak stiffness region: a series of modes for RWD and SS are proposed in the paper. In addition, the average maximum SS is slightly less than the corresponding deterministic result while the average maximum RWD is slightly larger than that in the deterministic calculation. These may be explained by the inhomogeneous distribution of the soil stiffness, especially in zones of weakness.
3. The effects of anisotropic random field: the effects of vertical *SOFs* on the excavation-induced responses are greater than those of horizontal *SOFs*. In the paper, the correlation of vertical *SOF* is proposed to explain that the most scattered result occurs when vertical *SOF* is close to the excavation size, which does not occur when investigating the influence of horizontal *SOF*.

In the present research, some useful conclusions have been drawn in the investigation of the excavation-induced deformations in spatially variable clays; however, only the first support of such a braced excavation is considered and the analysis of the base has not been involved, thus allowing scope for future research.

Acknowledgements This work was supported by National Natural Science Foundation of China (Grant Nos 51909259, 52079135, and 52008122), the International Partnership Program of Chinese Academy of Sciences (Grant No. 131551KYSB20180042), the Science and Technology R & D Project of China State Construction International Holdings Limited (No. CSCI-2020-Z-21), and Ningbo Public Welfare

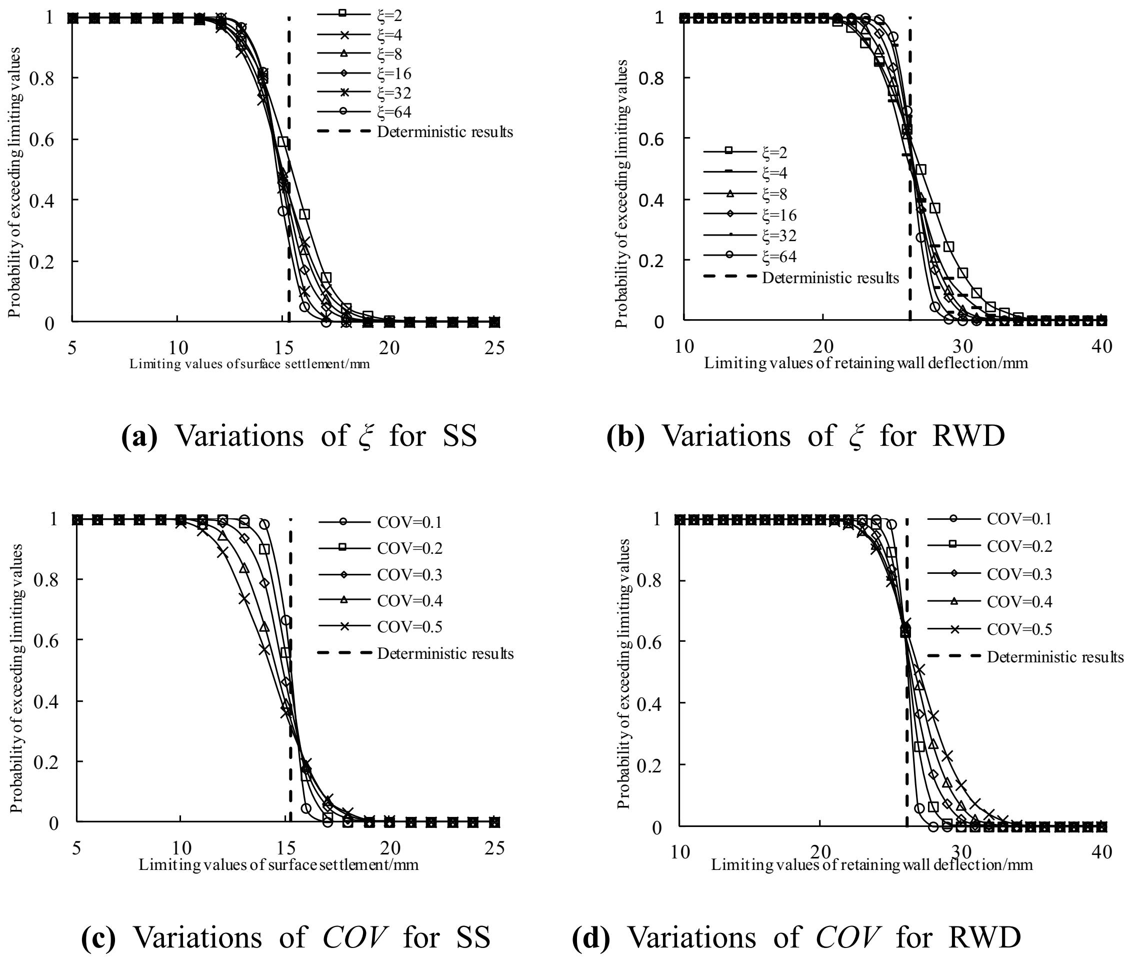

(a) Variations of ξ for SS **(b)** Variations of ξ for RWD

(c) Variations of COV for SS **(d)** Variations of COV for RWD

Fig. 18 Influences of spatial variability on the probability of exceeding the specified limiting deformations at various combinations of *SOF* (or ξ) and *COV*

Science and Technology Planning Project (No. 2019C50012). The authors are also grateful to the reviewers and editors for their valuable comments and suggestions.

References

1. Kung, G.T.C.; Hsiao, E.C.L.; Schuster, M.; Juang, C.H.: A neural network approach to estimating deflection of diaphragm walls caused by excavation in clays. Comput. Geotech. **34**(5), 385–396 (2007)
2. PSCG.: Specification for excavation in Shanghai metro construction. Shanghai, China: Professional Standards Compilation Group (2000)
3. Zheng, G.; Yang, X.; Zhou, H.; Du, Y.; Sun, J.; Yu, X.: A simplified prediction method for evaluating tunnel displacement induced by laterally adjacent excavations. Comput. Geotech. **95**(3), 119–128 (2018)
4. Kung, G.T.C.; Juang, C.H.; Hsiao, E.C.L.; Hashash, Y.M.A.: Simplified model for wall deflection and ground-surface settlement caused by braced excavation in clays. J. Geotech. Geoenviron. Eng. **133**(6), 731–747 (2007)
5. Zhang, W.G.; Goh, A.T.C.; Xuan, F.: A simple prediction model for wall deflection caused by braced excavation in clays. Comput. Geotech. **63**, 67–72 (2015)
6. Morgenstern, N.R.: Performance in geotechnical practice. HKIE Transactions **7**(2), 2–15 (2000)
7. Lumb, P.: The variability of natural soils. Can. Geotech. J. **3**(2), 74–97 (2011)
8. Vanmarcke, E.H.: Probabilistic modeling of soil profiles. J. Geotech. Eng. Div. **103**, 1227–12446 (1977)
9. Fenton, G.A.; Griffiths, D.V.: Three-dimensional probabilistic foundation settlement. J. Geotech. Geoenviron. Eng. **131**(2), 232–239 (2005)
10. Cheng, H.Z.; Chen, J.; Li, J.B.: Probabilistic Analysis of Ground Movements Caused by Tunneling in a Spatially Variable Soil. Int. J. Geomech. **19**(12), 04019125 (2019)
11. Griffiths, D.V.; Asce, F.; Huang, J.S.; Asce, M.; Fenton, G.A.: Influence of spatial variability on slope reliability using 2D random fields. J. Geotech. Geoenviron. Eng. **135**(10), 1367–1378 (2009)

12. Cheng, H.Z.; Chen, J.; Chen, R.P.; Chen, G.L.; Zhong, Y.: Risk assessment of slope failure considering the variability in soil properties. Comput. Geotech. **103**, 61–72 (2018)
13. Luo, Z.; Li, Y.; Zhou, S.; Di, H.: Effects of vertical spatial variability on supported excavations in sands considering multiple geotechnical and structural failure modes. Comput. Geotech. **95**, 16–29 (2018)
14. Ching, J.Y.; Phoon, K.K.; Sung, S.P.: Worst case scale of fluctuation in basal heave analysis involving spatially variable clays. Struct. Saf. **68**, 28–42 (2017)
15. Gholampour, A.; Johari, A.: Reliability-based analysis of braced excavation in unsaturated soils considering conditional spatial variability. Comput. Geotech. **115**, 103163 (2019)
16. Sert, S.; Luo, Z.; Xiao, J.; Gong, W.; Juang, C.H.: Probabilistic analysis of responses of cantilever wall-supported excavations in sands considering vertical spatial variability. Comput Geotech. **75**, 182–191 (2016)
17. Lo, M.K.; Leung, Y.F.: Bayesian updating of subsurface spatial variability for improved prediction of braced excavation response. Can. Geotech. J. **56**(8), 1169–1183 (2019)
18. Phoon, K.K.; Kulhawy, F.H.: Evaluation of geotechnical property variability. Can Geotech J. **129**(4), 625–639 (1999)
19. Phoon, K.K.; Kulhawy, F.H.: Characterization of geotechnical variability. Can. Geotech. J. **36**(4), 612–624 (1999)
20. El-Ramly, H.; Morgenstern, N.R.; Cruden, D.M.: Probabilistic stability analysis of a tailings dyke on presheared clay-shale. Can. Geotech. J. **40**(1), 192–208 (2003)
21. Zhang, W.G.; Li, Y.Q.; Wu, C.Z.; Li, H.R.; Goh, A.T.C.; Liu, H.L.: Prediction of lining response for twin tunnels constructed in anisotropic clay using machine learning techniques. Undergr. Space (2020)
22. Li, Y.Q.; Zhang, W.G.: Investigation on passive pile responses subject to adjacent tunnelling in anisotropic clay. Comput. Geotech. **127**(3), 103782 (2020)
23. Zhang, W.G.; Han, L.; Gu, X.; Wang, L.; Chen, F.Y.; Liu, H.L.: Tunneling and deep excavations in spatially variable soil and rock masses: A short review. Undergr. Space (2020)
24. Teng, F.C.; Ou, C.Y.; Hsieh, P.G.: Measurements and numerical simulations of inherent stiffness anisotropy in soft Taipei clay. J. Geotech. Geoenviron. Eng. **140**(1), 237–250 (2014)
25. Grimstad, G.; Andresen, L.: Jostad HP NGI-ADP: anisotropic shear strength model for clay. Int. J. Numer. Anal. Methods Geomech. **36**, 483–497 (2012)
26. Chen, G.H.; Zou, J.F.; Chen, J.Q.: Shallow tunnel face stability considering pore water pressure in non-homogeneous and anisotropic soils. Comput. Geotech. **116**, 103205 (2019)
27. Goh, A.T.C.; Zhang, R.H.; Wang, W.; Wang, L.; Liu, H.L.; Zhang, W.G.: Numerical study of the effects of groundwater drawdown on ground settlement for excavation in residual soils. Acta Geotech. (2019)
28. Zhang, R.H.; Wu, C.Z.; Goh, A.T.C.; Thomas, B.; Zhang, W.G.: Estimation of diaphragm wall deflections for deep braced excavation in anisotropy clays using ensemble learning. Geosci. Front. (2020)
29. Zhang, R.H.; Goh, A.T.C.; Li, Y.Q.; Hong, L.; Zhang, W.G.: Assessment of apparent earth pressure for braced excavations in anisotropic clay. Acta Geotech. 1–12 (2021)
30. Zhang, W.G.; Zhang, R.H.; Wu, C.Z.; Goh, A.T.C.; Wang, L.: Assessment of basal heave stability for braced excavations in anisotropic clay using extreme gradient boosting and random forest regression. Undergr. Space (2020)
31. Hsieh, P.G.; Ou, C.Y.; Liu, H.T.: Basal heave analysis of excavations with consideration of anisotropic undrained strength of clay. Can. Geotech. J. **45**(6), 788–799 (2008)
32. Kong, D.S.; Men, Y.Q.; Wang, L.H.; Zhang, Q.H.: Basal heave stability analysis of deep foundation pits in anisotropic soft clays. J. Cent. S. Univ. **43**(11), 4472–4476 (2012)
33. Puzrin, A.M.; Burland, J.B.: Non-linear model of small-strain behavior of soils. Geotechnique **48**(2), 217–233 (1998)
34. Burland, J.B.: Small is beautiful-the stiffness of soils at small strains. Can. Geotech. J. **26**, 499–516 (1989)
35. Benz, T.: Small-Strain Stiffness of Soils and Its Numerical Consequences. PhD thesis, Universität Stuttgart (2007)
36. Schweiger, H.F.; Vermeer, P.A.; Wehnert, M.: On the design of deep excavations based on finite element analysis. Geomech. Tunnell. **2**(4), 333–344 (2009)
37. Jin, Y.F.; Yin, Z.Y.; Zhou, W.H.; Huang, H.W.: Multi-objective optimization-based updating of predictions during excavation. Eng. Appl. Artif. Intell. **78**, 102–123 (2019)
38. Zhang, D.M.; Xie, X.C.; Li, Z.L.; Zhang, J.: Simplified analysis method for predicting the influence of deep excavation on existing tunnels. Comput. Geotech. **121**, 103477 (2020)
39. FLAC3D (Fast Lagrangian Analysis of Continua in 3 Dimensions), Version 6.0, User manual. USA: ltasca Consulting Group, Inc (2017)
40. Wang, W.D.; Wang, H.R.; Xu, Z.H.: Study of parameters of HS-small model used in numerical analysis of excavations in Shanghai area. Rock Soil Mech. **83**(5), 413–419 (2013)
41. Davis, M.W.: Production of conditional simulations via the LU triangular decomposition of the covariance matrix. Math. Geol. **19**(2), 91–98 (1987)
42. Fenton, G.A.; Griffiths, D.V.: Probabilistic foundation settlement on spatially random soil. J. Geotech. Geoenviron. Eng. **128**(5), 381–390 (2002)